The Astronomical Journal, 157:102 (15pp), 2019 March https://doi.org/10.3847/1538-3881/aaff69

Spitzer Transit Follow-up of Planet Candidates from the *K2* Mission

John H. Livingston[1,17], Ian J. M. Crossfield[2], Michael W. Werner[3], Varoujan Gorjian[3], Erik A. Petigura[4,18], David R. Ciardi[5], Courtney D. Dressing[6], Benjamin J. Fulton[7], Teruyuki Hirano[8], Joshua E. Schlieder[9], Evan Sinukoff[4,10], Molly Kosiarek[11,19], Rachel Akeson[5], Charles A. Beichman[5], Björn Benneke[12], Jessie L. Christiansen[5], Bradley M. S. Hansen[13], Andrew W. Howard[4], Howard Isaacson[6], Heather A. Knutson[7], Jessica Krick[5], Arturo O. Martinez[14], Bun'ei Sato[8], and Motohide Tamura[1,15,16]

[1] Department of Astronomy, University of Tokyo, 7-3-1 Hongo, Bunkyo-ku, Tokyo 113-0033, Japan; livingston@astron.s.u-tokyo.ac.jp
[2] Department of Physics, Massachusetts Institute of Technology, Cambridge, MA 02139, USA
[3] Jet Propulsion Laboratory, 4800 Oak Grove Drive, Pasadena, CA 91109, USA
[4] Department of Astronomy, California Institute of Technology, 1200 E. California Boulevard, Pasadena, CA 91125, USA
[5] Caltech/IPAC-NASA Exoplanet Science Institute, 1200 E. California Boulevard, Pasadena, CA 91125, USA
[6] Astronomy Department, University of California, Berkeley, CA 94720, USA
[7] Geological and Planetary Sciences, California Institute of Technology, 1200 E. California Boulevard, Pasadena, CA 91125, USA
[8] Department of Earth and Planetary Sciences, Tokyo Institute of Technology, 2-12-1 Ookayama, Meguro-ku, Tokyo 152-8551, Japan
[9] NASA Goddard Space Flight Center, 8800 Greenbelt Road, Greenbelt, MD 20771, USA
[10] Institute for Astronomy, University of Hawai'i at Mānoa, Honolulu, HI, USA
[11] Department of Astronomy, University of California, Santa Cruz, Santa Cruz, CA, USA
[12] Département de Physique, Université de Montréal, Montréal, QC H3C 3J7, Canada
[13] Mani L. Bhaumik Institute for Theoretical Physics, Department of Physics & Astronomy, University of California Los Angeles, Los Angeles, CA 90095, USA
[14] Department of Physics and Astronomy, Georgia State University, 25 Park Place NE, Atlanta, GA 30303, USA
[15] Astrobiology Center, NINS, 2-21-1 Osawa, Mitaka, Tokyo 181-8588, Japan
[16] National Astronomical Observatory of Japan, NINS, 2-21-1 Osawa, Mitaka, Tokyo 181-8588, Japan
Received 2018 March 23; revised 2019 January 8; accepted 2019 January 14; published 2019 February 8

Abstract

We present precision 4.5 μm *Spitzer* transit photometry of eight planet candidates discovered by the *K2* mission: K2-52 b, K2-53 b, EPIC 205084841.01, K2-289 b, K2-174 b, K2-87 b, K2-90 b, and K2-124 b. The sample includes four sub-Neptunes and two sub-Saturns, with radii between 2.6 and 18 $R_\oplus$ and equilibrium temperatures between 440 and 2000 K. In this paper we identify several targets of potential interest for future characterization studies, demonstrate the utility of transit follow-up observations for planet validation and ephemeris refinement, and present new imaging and spectroscopy data. Our simultaneous analysis of the *K2* and *Spitzer* light curves yields improved estimates of the planet radii and multiwavelength information that helps validate their planetary nature, including the previously unvalidated candidate EPIC 205686202.01 (K2-289 b). Our *Spitzer* observations yield an order-of-magnitude increase in ephemeris precision, thus paving the way for efficient future study of these interesting systems by reducing the typical transit timing uncertainty in mid-2021 from several hours to a dozen or so minutes. K2-53 b, K2-289 b, K2-174 b, K2-87 b, and K2-90 b are promising radial velocity (RV) targets given the performance of spectrographs available today or in development, and the M3V star K2-124 hosts a temperate sub-Neptune that is potentially a good target for both RV and atmospheric characterization studies.

Key words: planets and satellites: detection – planets and satellites: fundamental parameters – techniques: photometric

1. Introduction

The NASA *K2* mission (Howell et al. 2014) has extended the legacy of *Kepler* by discovering transiting exoplanets and candidate planets at a rate of hundreds per year. In contrast to *Kepler*, *K2* surveyed a wider sky area at the cost of shorter time baseline per field, which has enabled the discovery of planets orbiting brighter stars. In addition to monitoring a greater number of bright stars than *Kepler*, *K2* monitored more low-mass stars than *Kepler*, partly as a result of its community-driven target selection. The result is that planets detected by *K2* are generally more amenable to follow-up. To date, *K2* has significantly enhanced the number of known small planets orbiting brighter stars than those surveyed by *Kepler* (Foreman-Mackey et al. 2015; Montet et al. 2015; Vanderburg et al. 2016; Crossfield et al. 2016; hereafter Cr16; Livingston et al. 2018a, 2018c; Mayo et al. 2018), as well as discovering planets in cluster environments (David et al. 2016a; Mann et al. 2016a, 2017, 2018; Obermeier et al. 2016; Gaidos et al. 2017; Pepper et al. 2017; Ciardi et al. 2018; Livingston et al. 2018b, 2019; Rizzuto et al. 2018), including a 5–10 Myr planet in the Upper Scorpius star-forming region (David et al. 2016b; Mann et al. 2016b). *K2* planets will be available for follow-up studies with the *James Webb Space Telescope* (*JWST*; Gardner et al. 2006) contemporaneously with the planets expected to be found by the *Transiting Exoplanet Survey Satellite* (*TESS*; Ricker et al. 2015).

Our focus with *Spitzer* (Werner et al. 2004) is on small planets orbiting K and M dwarfs discovered by *K2*, which could potentially be good targets for future radial velocity (RV) or atmospheric characterization studies. We have been conducting *Spitzer* transit observations of planet candidates and using these data to refine estimates of their orbital and physical parameters. As *K2* observes each field for approximately 80 days each, our observations play a critical role in refining the ephemerides owing to the long time baseline they provide (typically 6–12

[17] JSPS Fellow.
[18] Hubble Fellow.
[19] NSF Graduate Research Fellow.

months longer). These results are part of an ongoing program, data from which have been used to ensure the feasibility of future study of *K2* planets by Beichman et al. (2016), Benneke et al. (2017), Chen et al. (2018), Dressing et al. (2018), and K. Hardegree-Ullman et al. (2019, in preparation).

In this paper we validate the planet K2-289 b, identify several targets of potential interest for future characterization studies, and demonstrate the utility of transit follow-up observations for ephemeris refinement. When done with a smaller beam, i.e., with *Spitzer* or *CHEOPS* (Fortier et al. 2014), such follow-up will prove especially useful in the validation of planet candidates identified by *TESS*, which will frequently encounter stellar blends owing to the $\sim 21''$ pixel scale of its detectors. In Section 2 we describe our observations, including *K2* and *Spitzer* photometry, high-resolution imaging and spectroscopy, and literature data. In Section 3 we describe the analysis methods used to measure host star and planet properties from these data, as well as our planet validation approach. In Section 4 we present the results of our analyses and discuss the potential for future characterization studies, and we conclude with a summary in Section 5.

2. Observations

2.1. K2 *Photometry*

The basis for this work is the initial identification of planet candidates in *K2* light curves. This process is described in Cr16 and Petigura et al. (2018), but we briefly summarize it here. We use `k2phot`[20] to correct the instrumental systematics induced by the roll of the *Kepler* spacecraft. The resulting corrected light curves are publicly available on the community portal ExoFOP.[21] We use `TERRA`[22] to search these light curves for transit signals, and the resulting candidates are then vetted by eye to eliminate instrumental or astrophysical false positives (FPs). During this process, we also assess the utility of conducting follow-up transit observations with *Spitzer*. The planets we analyze here were all deemed interesting targets for *Spitzer* because they are relatively small, are temperate, and/or orbit late-type host stars. All of the planets and candidates in this work were previously published by Cr16, with the exception of K2-124 b, which was observed in *K2* Campaign 5 and subsequently discovered by our team (Dressing et al. 2017; Livingston et al. 2018a; Petigura et al. 2018).

2.2. Spitzer *Photometry*

Spitzer presents several advantages over ground-based transit follow-up observations: its position in space enables precise photometry unaffected by Earth's atmosphere, its Earth-trailing orbit frees it from the scheduling constraints imposed by the day/night cycle on Earth, the diminished effects of limb darkening in the infrared enable precise estimation of transit model parameters, and the 4.5 μm Infrared Array Camera (IRAC; Fazio et al. 1998) bandpass (in conjunction with the *Kepler* bandpass) provides a relatively broad wavelength baseline that facilitates planet validation. In addition, our high-cadence *Spitzer* observations provide better sampling of the transit than the 30-minute cadence of *K2*.

[20] https://github.com/petigura/k2phot
[21] https://exofop.ipac.caltech.edu
[22] https://github.com/petigura/terra

Table 1
Spitzer Observing Log

EPIC	Name	Int. Time (s)	Duration (hr)	Start Date (JD)
203776696	K2-52	30	10.6	2,457,337.6776
204890128	K2-53	6	8.1	2,457,347.8974
205084841		30	7.8	2,457,334.7969
205686202	K2-289	12	8.9	2,457,554.5479
210558622	K2-174	2[a]	13.5	2,457,533.4483
210731500	K2-87	30	11.8	2,457,519.4901
210968143	K2-90	12	10.4	2,457,531.5406
212154564	K2-124	30	8.3	2,457,590.9404

Note.
[a] Due to the brightness of K2-174, the observations were conducted in subarray mode to accommodate shorter integrations and limit the bandwidth required for the data downlink to Earth.

We conducted our transit observations using the IRAC 4.5 μm channel as part of *Spitzer* cycle 11 GO program 11026 (PI: Werner). We chose integration times between 2 and 30 s to keep the detector in the linear regime and minimize downlink bandwidth. Target acquisition places the stars on the "sweet spot" of the detector, which has been well characterized for the purpose of precise time-series photometry (Ingalls et al. 2012) and falls within the region of the detector accessible in subarray mode (used for observing bright stars). Following the guidelines for high-precision *Spitzer* photometry (Grillmair et al. 2012), we performed $\sim$30 minutes of integrations on an empty field before each transit observation, which can help mitigate systematics induced by thermal settling of the spacecraft. See Table 1 for details of the observations.

2.3. *High-resolution Imaging*

High-resolution imaging is important for detecting stellar companions and constraining the probability of chance alignments with background sources within the *K2* and *Spitzer* photometric apertures and thus plays a critical role in assessing the false-positive probability (FPP) of a planet candidate. In this work, we utilize imaging previously published by Cr16 along with additional AO imaging from Keck/NIRC2 (Wizinowich et al. 2014). Cr16 did not obtain imaging of EPIC 205084841, so we used NIRC2 in natural guide star mode to observe the star in *K* band on UT 2017 July 9. Using the image reduction and analysis methods described in Cr16, we find the star to be single and rule out companions above the contrast curve shown in Figure 1 at the 5σ confidence level. We also utilize a *J*-band image of K2-289, which was obtained with NIRC2 on UT 2015 April 1 and made available on ExoFOP but was not published in Cr16. As in the *K* -band image reported by Cr16, the companion is clearly detected in *J* band, thus providing useful color information (see Section 4.1).

2.4. *Spectroscopy*

Our team has primarily used Keck/HIRES (Vogt et al. 1994) to obtain high-resolution spectra of candidate host stars, enabling the measurement of more robust planet properties, as well as detecting (or ruling out) double-lined spectroscopic binaries (see Cr16 and Petigura et al. 2018 for more details). We use `SpecMatch-syn` to measure precise stellar parameters from the spectra of stars hotter than $\sim$4200 K, which matches spectra

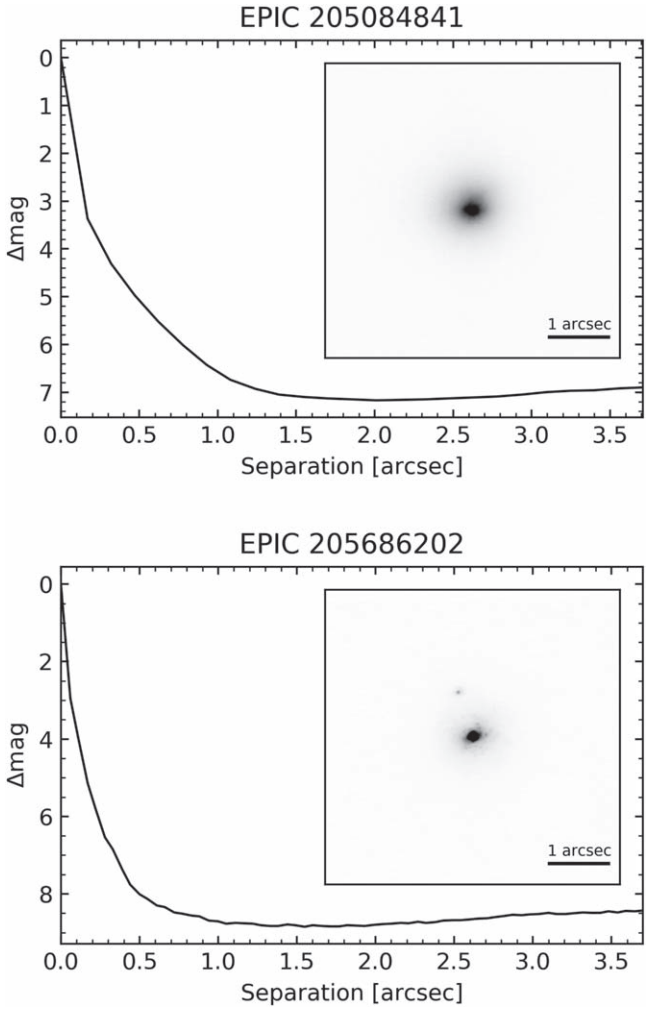

Figure 1. Keck/NIRC2 *K*-band AO imaging of EPIC 205084841 and EPIC 205686202 (K2-289) and their resulting contrast curves.

to an interpolated grid of models from Coelho et al. (2005). For cooler stars, we use `SpecMatch-emp`, which matches spectra to a spectral library of 404 standard stars (Yee et al. 2017a).

We also conducted spectroscopic observations of K2-289 using the High Dispersion Spectrograph (HDS) mounted on the Subaru 8.2 m telescope between UT 2016 April 29 and May 2. We employed the standard I2a setup, which covers 4940–7590 Å, and image slicer #2, achieving a spectral resolution of $R \sim 80{,}000$. For the RV measurements, we used the iodine (I_2) cell on three consecutive nights. We also obtained the stellar spectrum without the I_2 cell for the template of RV measurements. The HDS data were reduced using standard IRAF routines, by which we extracted one-dimensional, wavelength-calibrated spectra of K2-289. We then put those spectra through an RV analysis pipeline (Sato et al. 2002, 2012), which does a forward modeling of each observed spectrum to measure the RV relative to the template. Table 2 lists the extracted relative RVs and their internal errors.

Table 2
Radial Velocities of K2-289 Obtained with Subaru/HDS

BJD	RV (Relative) ($m\ s^{-1}$)	Error ($m\ s^{-1}$)
2,457,509.063075	−5.95	23.95
2,457,510.065150	21.30	21.79
2,457,510.086821	62.27	22.18
2,457,511.067174	−10.08	21.78
2,457,511.088864	−16.61	24.39

3. Analysis

3.1. K2 *Light Curves*

As part of our team's large-scale transit search of the *K2* data (Section 2.1), we correct systematics induced by the coupling of spacecraft motion and intrapixel gain variations with `k2phot`, which uses a Gaussian Process model (GP; Rasmussen & Williams 2005). The resulting light curves are essentially free of the large-amplitude position-dependent flux variations characteristic of raw *K2* photometry, but stellar variability and potentially residual systematic trends must be accounted for to measure precise transit properties. A common approach is to first model and remove out-of-transit variability using various methods, such as a median filter, polynomial, or spline model. These approaches are simple and fast and usually do not significantly impact the results for stars with low levels of variability and residual systematics. In order to minimize the potential for biased parameter estimates while employing a uniform framework for a range of light-curve behaviors, we use the `celerite` GP framework with a Matern-3/2 kernel and take an approach similar to the "type II" maximum likelihood estimation (MLE) described in Gibson et al. (2012).

The GP is first trained on the out-of-transit light curve using `scipy.optimize`, and then the full light curve is analyzed with the same GP in conjunction with the transit model (Section 3.4). We first use the "L-BFGS-B" method (Byrd et al. 1995; Zhu et al. 1997) to find the MLE value of the kernel hyperparameters given the out-of-transit light curve, using the GP likelihood and gradient in `celerite`. During this stage, we perform iterative outlier rejection to minimize the possibility of biased kernel hyperparameters. Next, we use the Nelder–Mead simplex algorithm (Nelder & Mead 1965) to fit the joint GP and transit model to the full light curve, initialized with the MLE kernel hyperparameters and an initial set of transit parameters from previous analyses. Fitting the GP hyperparameters simultaneously with the transit model helps ensure that we find an optimal noise model that is valid during and out of transit. We then restrict the data to 1-day windows centered on each transit and sample the posterior of the joint GP-transit model, by running `emcee` for 500 steps initialized with the optimum found in the previous step. This brief sampling stage is especially important if the kernel hyperparameters are initially stuck in a local optimum, and it can be used to ensure that the posteriors are unimodal and sharply peaked around these optimal values.

Finally, we fix the hyperparameters to their optima and proceed to run the sampler for 10,000 steps (see also Section 3.4). This approach retains the benefits of a flexible noise model while minimizing computational complexity. Figures 2 and 3 show examples of these fits, with data points shown in gray if they were excluded during the iterative outlier rejection performed during the initial GP training stage.

3.2. Spitzer *Light-curve Extraction*

We extract the *Spitzer* light curves following the approach taken by Knutson et al. (2012) and Beichman et al. (2016). In brief, we compute aperture photometry using circular apertures

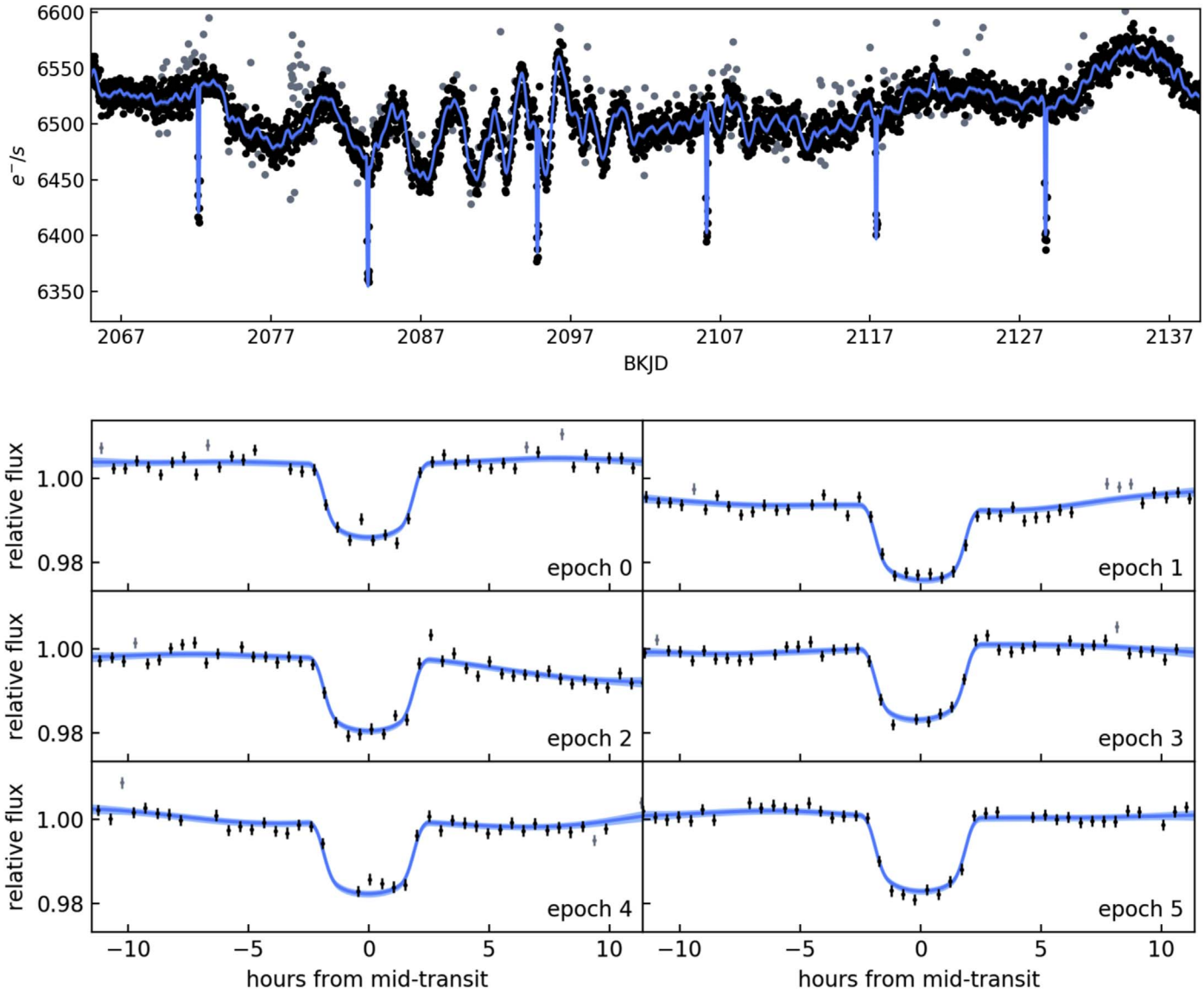

Figure 2. Top: *K2* photometry of EPIC 205084841 from `k2phot` with the best-fit GP model and the GP-detrended light curve with best-fit transit model. Bottom: individual transits in the *K2* light curve with the best-fit GP and transit models to illustrate the quality of the detrending in the top panel. In all panels the data are shown in black, outliers are shown in gray, models are shown in blue, and the shaded blue regions show the 2σ uncertainty from the GP model.

centered on the host star, for a range of radii between 2.0 and 5.0 pixels, corresponding to 2.″4–6.″0 owing to *Spitzer*'s 1.″2 pixel scale. We used a step size of 0.1 pixels from 2.0 to 3.0 and a step size of 0.5 from 3.0 and 5.0. An important component of precision photometry with *Spitzer* is the selection of an optimal aperture, due to the fact that significant levels of "red" (correlated) noise are present to a varying extent in each time series. Smaller radii tend to have less photon noise owing to the decreased sky background in the aperture, while slightly larger radii can sometimes mitigate the inter- and intrapixel gain variations that are responsible for the correlated noise. Ideally, an optimal radius minimizes both of these effects, although in practice it is common to attempt only to minimize correlated noise or the photon noise (e.g., Knutson et al. 2012; Lewis et al. 2013; Lanotte et al. 2014).

A typical transit data set contains significant time both in and out of transit, so we compute relevant noise metrics as a function of radius for different subsets, most of which are fully out of transit or between second and third contact (i.e., do not contain ingress or egress). Thus, for a given radius, the ensemble of these values is largely unaffected by the transit signal and thus reflects only photon noise and systematic noise. To quantify the level of red noise, we compute β, the factor by which the standard deviation of the observed binned residuals deviates from the theoretical value (Pont et al. 2006; Winn et al. 2008):

$$\beta = \frac{\sigma_M}{\sigma_0}\sqrt{\frac{N(M-1)}{M}}, \quad (1)$$

where σ_M is the standard deviation of the binned residuals (in M bins), σ_0 is the standard deviation of the unbinned residuals, and N is the number of data points per bin. To ensure a robust estimate and focus on the timescales of red noise that could significantly impact transit parameter estimates, we compute the median β value for bin widths between 5 and 40 minutes. We divide each flux time series into 10 equal-sized segments and compute both the standard deviation (i.e., overall noise level) and the β value (i.e., red-noise level) for each segment. The

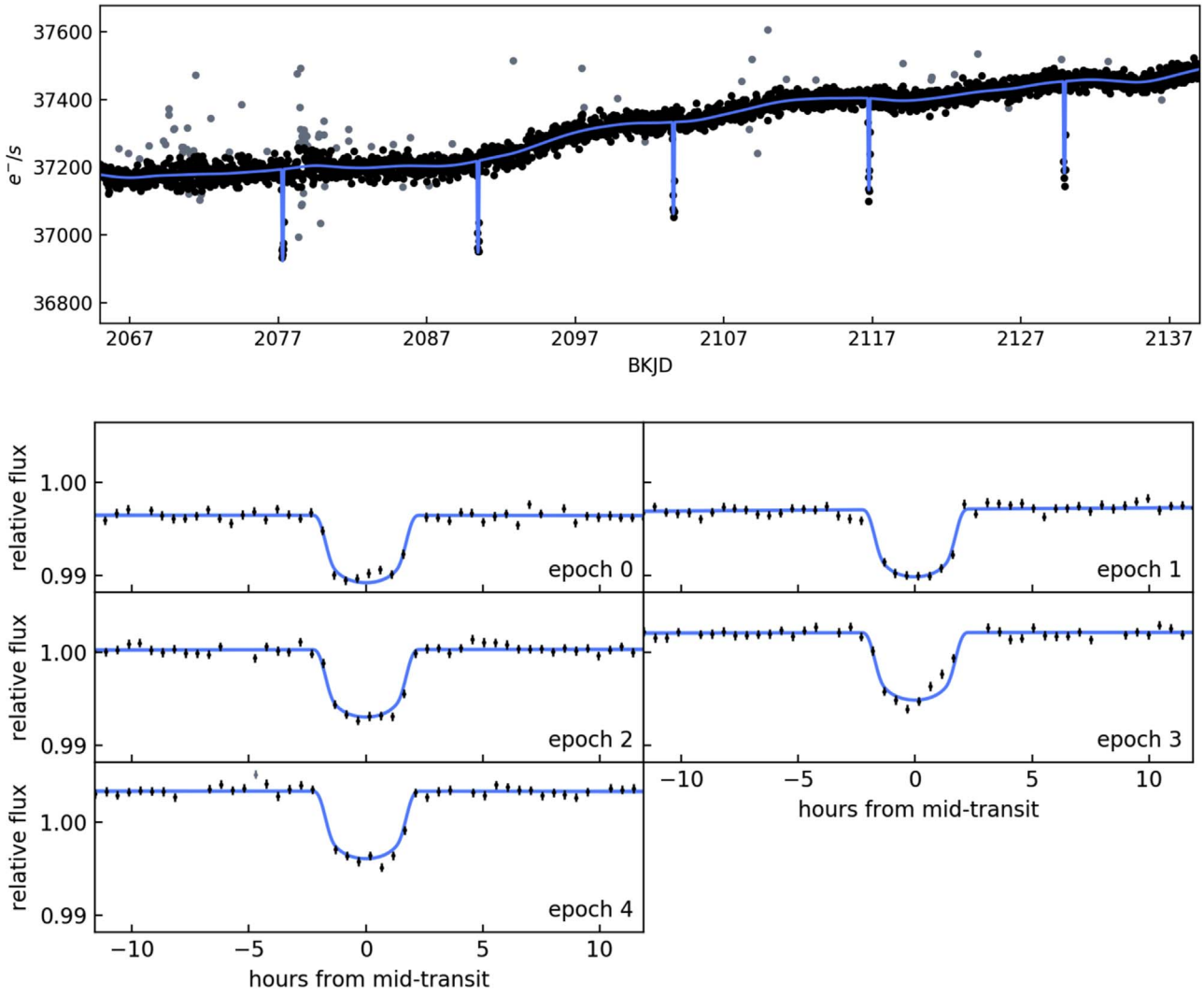

Figure 3. Same as Figure 2, but for K2-289 b. In-transit variability could be the result of spot-crossing, or simply residual systematics. An increase in the number of outliers can be seen near BKJD = 2079 in this light curve, as well as the one in Figure 2, which suggests an instrumental origin.

optimal aperture is then the one that minimizes each metric. We then compute the median of the optimal aperture radii for each metric over all segments. Finally, the aperture radius adopted for subsequent analysis is the mean of these two "optimal" radii; the selected aperture thus only "approximately" minimizes both metrics in cases where these two radii are not equal. We chose 10 segments as a trade-off between having more robust statistics and having enough light curve in each segment to compute red noise on a range of different timescales. We find that the minimum red-noise aperture is frequently consistent with the minimum standard deviation aperture to within a few tenths of a pixel, and the optimal radius is typically 2.2–2.4 pixels, which is consistent with the optimal apertures found in previous analyses of *Spitzer* transit data (e.g., Knutson et al. 2012), in which the residuals computed from the best-fit transit and systematics model are analyzed instead of the raw light curve.

In principle, aperture selection could be handled via Bayesian model selection (i.e., computing the Bayesian evidence), although any improvements might not be significant enough to justify the computational cost. Additionally, it may be fruitful to simultaneously estimate the white- and red-noise levels using a GP; a sufficient choice of kernel could more fully disentangle these two noise signals, as compared to the standard deviation and β factor. We leave an investigation of these possibilities for a future work.

3.3. Spitzer *Systematics Model*

We model the systematics inherent to the *Spitzer* light curves using the pixel-level decorrelation (PLD) method (Deming et al. 2015). In comparisons between various methods used to correct *Spitzer* systematics (Ingalls et al. 2016), PLD was among the top performers, displaying both high precision and repeatability. PLD uses a linear combination of (normalized) pixel light curves to model the effect of point-spread function (PSF) motion on the detector coupled with intrapixel gain variations; thus, it does not require the calculation of centroids. The parameterization of the full model for the transit light curve, including PLD, is

$$\Delta S^t = \frac{\sum_{i=1}^{9} c_i P_i^t}{\sum_{i=1}^{9} P_i^t} + M_{\rm tr}(\boldsymbol{\theta}, t) + \varepsilon(\sigma), \quad (2)$$

where $M_{\rm tr}$ is the transit model, c_i are the PLD coefficients, and $\varepsilon(\sigma)$ are zero-mean Gaussian errors with width σ. To form a valid set of basis vectors for the instrumental systematics

component of the light curve, the astrophysical signal in each individual pixel light curve is removed by normalization (the sum in the denominator of Equation (2)). We show an illustrative example of these normalized pixel light curves in Figure 4. In testing, we found that using a 3×3 pixel grid sufficiently captures the information content corresponding to the motion of the PSF on the detector (which is typically $\lesssim$ a few tenths of a pixel). However, *Spitzer* target acquisition occasionally misses the "sweet spot" pixel, which may yield data sets with more pronounced systematics that could benefit from using a larger pixel grid (such as 5×5). In Figure 5 we plot the full model fit for two data sets (top panels), as well as the data corrected by subtracting the best-fit PLD noise model (bottom panels). In Figure 6 we plot the corrected data and transit models for the remaining *Spitzer* data sets.

3.4. Transit Fitting

To model the transits in both the *K2* and *Spitzer* light curves, we use the analytic model of Mandel & Agol (2002), assuming a circular orbit and a quadratic limb-darkening law, as implemented in `batman`. The free parameters $\boldsymbol{\theta}$ of the transit model are the planet-to-star radius ratio $R_p/R_\star$, scaled semimajor axis $a/R_\star$, midtransit time T_0, orbital period P, impact parameter $b \equiv a\cos(i)/R_\star$, and modified quadratic limb-darkening coefficients q_1 and q_2, which efficiently sample the space of physically allowed limb-darkening coefficients using the triangular sampling method of Kipping (2013). These transformed coefficients are computed directly from the quadratic limb-darkening coefficients u_1 and u_2 using Equations (17) and (18) of Kipping (2013), reproduced here for convenience:

$$q_1 \equiv (u_1 + u_2)^2, \tag{3}$$

$$q_2 \equiv \frac{u_1}{2(u_1 + u_2)}. \tag{4}$$

Following Cr16, we use Gaussian limb-darkening priors in our light-curve analysis, which we derive from the coefficients for the *Kepler* and IRAC bandpasses tabulated by Claret et al. (2012). We use a Monte Carlo approach in which we sample the stellar parameters ($T_{\rm eff}$, $\log g$, [Fe/H]) of each star and interpolate the tabulated coefficients at the sampled stellar values. Because we sample in q-space, we convert the tabulated values of u_1/u_2 to q_1/q_2 to enable using a Gaussian prior in q-space. We then use the mean and standard deviation of the sampled coefficients to define the Gaussian priors (see the Appendix for more details). For the final set of parameter estimates listed in Table 3 we also impose a prior on the mean stellar density determined from our `isochrones` analysis (see Section 3.7), which yields more precise parameter estimates by leveraging more information about the host star. However, we also perform a parallel set of identical analyses without this prior, which provides the opportunity to compare the density from our stellar characterization to the independent measurement of the mean stellar density from the light curve $\rho_{\star,\rm LC}$ (see Equation (7)). We discuss this in detail in Section 4.1.

For Markov chain Monte Carlo (MCMC) parameter estimation, we use `emcee`, a Python implementation of the affine-invariant ensemble sampler (Goodman & Weare 2010). We performed an initial optimization with `lmfit` and positioned 128 "walkers" in a Gaussian ball centered on the optimum. We then ran the sampler for 10,000 steps, allowing it to evolve according to the MCMC. Finally, we checked for convergence by visual inspection of the trace, discarding the first 5000 samples as "burn-in," and computed the autocorrelation time of each parameter using the Python package `acor`,[23] to ensure we had collected a sufficient number of independent samples after burn-in.

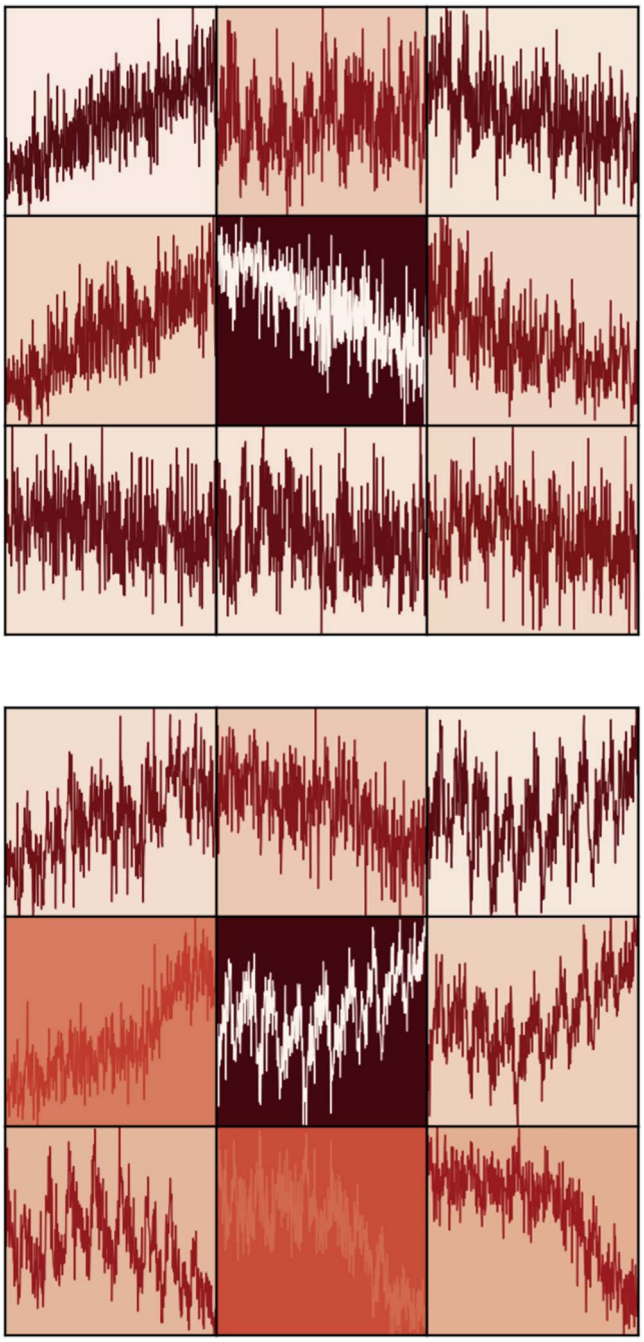

Figure 4. Normalized PLD pixel light curves of EPIC 205084841 (top) and K2-289 (bottom), displayed in a grid corresponding to their location on the detector, with time on the x-axis. The color of the background of each cell illustrates the relative intensity of each pixel, where lighter colors correspond to higher intensity.

3.5. Simultaneous K2 and Spitzer Analysis

In this work we simultaneously model the *K2* and *Spitzer* light curves of each target. This is motivated by several factors.

[23] https://github.com/dfm/acor

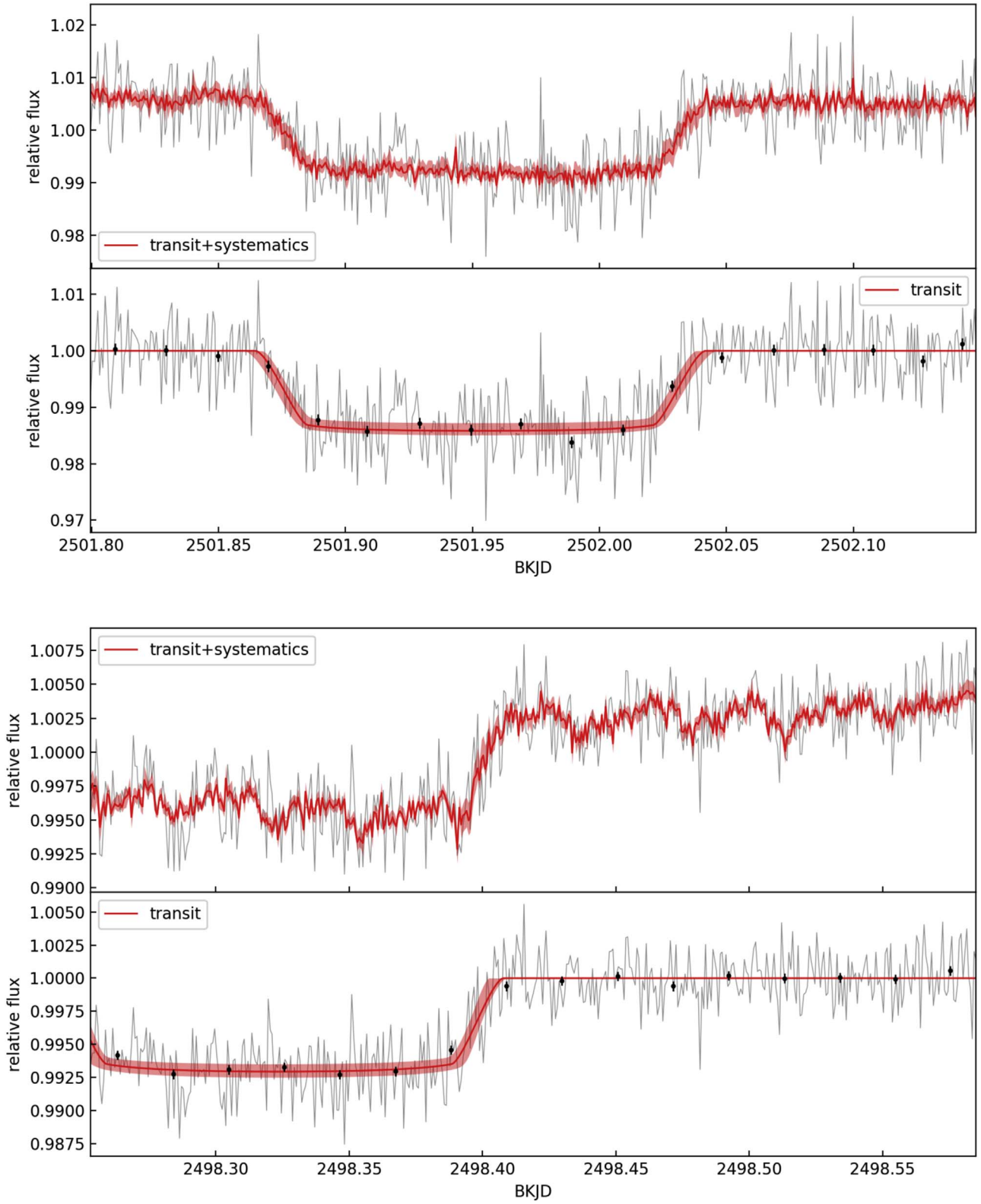

Figure 5. Best fit to the *Spitzer* EPIC 205084841.01 (top) and K2-289 b (bottom) light curves. The top panels show the raw light curve with the best-fitting model (transit + systematics) overplotted, normalized to the median flux during the observations. The bottom panels show the data with the best-fitting systematics component removed and the best-fitting transit model overplotted, normalized to unity out-of-transit flux. The 95% credible regions from our MCMC analysis are shown as shaded regions. To aid comparison with the *K2* data, the systematics-corrected photometry is also binned to the ∼30-minute *K2* observing cadence and shown as gray points, with error bars illustrating the Gaussian noise from the fit (scaled appropriately for the bin size).

First, the posterior distributions of some transit model parameters are often distinctly non-Gaussian (e.g., $a/R_\star$), so simply imposing Gaussian priors derived from previous analysis of the *K2* light curves could bias the resulting fits to the *Spitzer* data. Second, we leverage the *K2* data to model the *Spitzer* data, because we simultaneously fit the systematics and

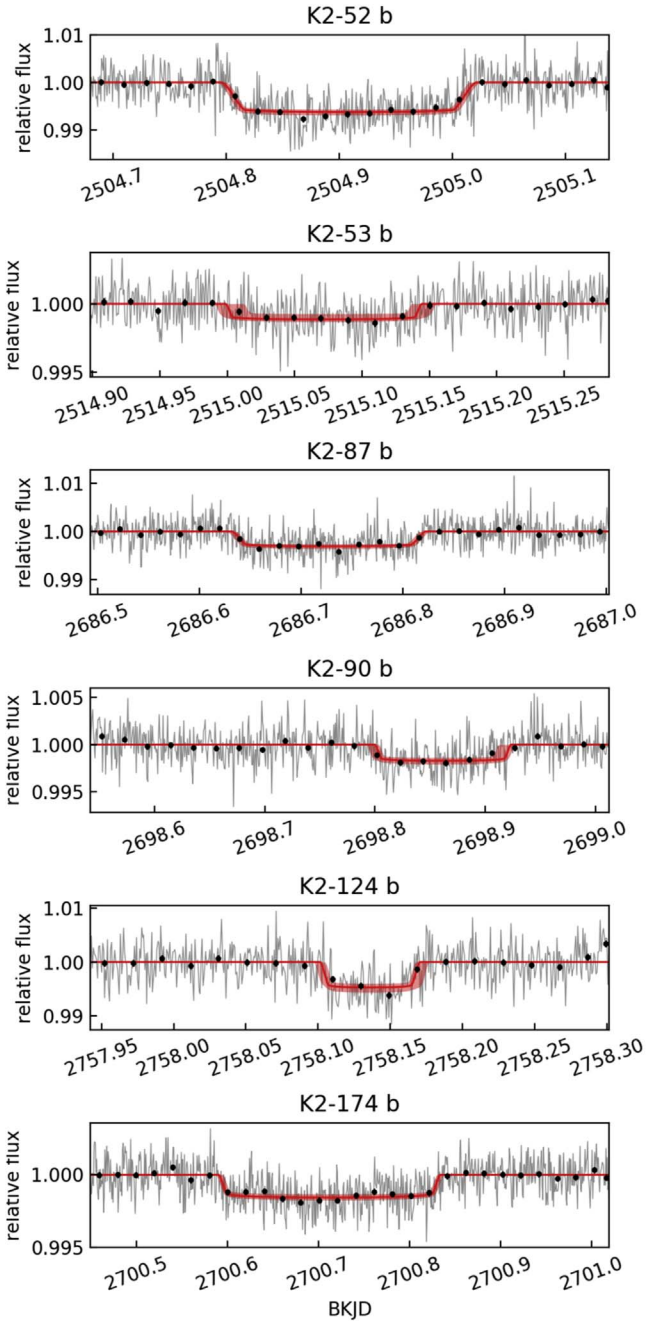

Figure 6. Same as the bottom panels of Figure 5, but for the remaining data sets.

transit models. Some transit model parameters ($a/R_\star$ and b) are shared between *Spitzer* and *K2*, while others are distinct. We fit $R_p/R_\star$ separately for the *Kepler* and *Spitzer* bandpasses to enable the detection of FP scenarios (see, e.g., Figure 7).

Our procedure is as follows. We first fit the *K2* data alone and form Gaussian priors on T_0 and P based on the mean and standard deviation of the posterior distributions from MCMC. These priors are then used in a fit to the *Spitzer* transit data alone, yielding an initial set of parameter estimates derived from the *Spitzer* data. We then fit the *K2* and *Spitzer* data simultaneously, without priors on T_0 and P. This simultaneous fit is responsible for the improvement in the ephemeris estimates, for reasons discussed above, as well as more robust transit shape parameter estimates. We list the transit parameters in Table 3 and the ephemeris estimates in Table 4.

An additional benefit to this approach is that it allows the high cadence and diminished limb darkening of our *Spitzer* light curves to yield improved constraints on transit parameters that are sensitive to ingress and egress (e.g., the impact parameter b). For example, even though our *Spitzer* observation (just barely) missed the ingress of K2-289 b (see Figure 5), the joint analysis of the *K2* and *Spitzer* data yields better constraints on the transit geometry than either the *Spitzer*-only or *K2*-only analyses. Figure 8 shows several key posterior distributions for this system from *K2*-only, *Spitzer*-only, and our joint analysis of both data sets, illustrating the improved constraints in transit geometry. The leftmost panels of Figure 8 show the stellar density from our `isochrones` analysis as gray bands for comparison to the mean stellar density derived from Equation (7) and the transit fit posteriors (without a density prior). In this case the density estimated from the *K2* data alone can be seen to be in mild disagreement with the `isochrones` density, but the *Spitzer* data yield an improved density estimate in good agreement. The improvement in parameter estimates afforded by this simultaneous modeling approach can be thought of as a type of "Bayesian shrinkage," in which the high cadence of *Spitzer* and high photometric precision of *K2* work together to extract higher measurement precision from the data.

3.6. Ephemerides

The addition of even a single follow-up transit measurement can result in significant refinement to the ephemeris of *K2* planet candidates, due to the relatively small number of transits detected in each ∼80-day *K2* observing campaign. The ephemerides from our simultaneous fit to the *K2* and *Spitzer* data are often a highly significant improvement over the *K2*-only ephemerides. To quantify this improvement, we compute the factor by which the precision on the estimate of the orbital period increases between the *K2*-only and joint fits to the *K2* and *Spitzer* data, which ranges from 8× to 13× (see Table 4).

The benefits of updating the ephemeris can be especially important in the context of planning future transit observations. Large uncertainties in the ephemeris estimates from the *K2* light curves are common, due to the relatively short time span of each *K2* observing campaign. The problem is particularly pronounced for planets with longer periods, which may transit only a small number of times in a given campaign. For those interested in studying the atmospheres of these planets, this complicates scheduling of future transit observations, due to the need to lengthen the observation window to ensure that the transit is fully observed.

However, the addition of a single transit observation with *Spitzer* dramatically reduces the length of the necessary observation windows in the *JWST* era. First, the longer time baseline yields an order-of-magnitude improvement in the precision of our orbital period estimates. Second, the new, combined transit midtime results in smaller propagated timing uncertainties as a result of being closer in time to the planned transit observation than the *K2* epoch. Our *Spitzer* observations reduce the typical uncertainty on the predicted transit time in mid-2021 from hours to minutes (see Table 4), enabling follow-up observations to be much more efficiently scheduled; even in 2025, the uncertainties will still be less than an hour.

Table 3
Transit Parameter Estimates

Name	a ($R_\star$)	b	i (deg)	$R_{p,K}$ ($R_\star$)	$R_{p,S}$ ($R_\star$)	$R_{p,C}$ ($R_\star$)	$\log(\sigma_K)$	$\log(\sigma_S)$	T_{14} (days)	T_{23} (days)	η	$R_{p,\max}$ ($R_\star$)
K2-52 b	$5.2^{+0.2}_{-0.3}$	$0.32^{+0.14}_{-0.18}$	$86.46^{+2.04}_{-1.91}$	$0.072^{+0.001}_{-0.001}$	$0.078^{+0.002}_{-0.002}$	$0.075^{+0.001}_{-0.001}$	−7.01	−5.70	$0.222^{+0.003}_{-0.003}$	$0.187^{+0.002}_{-0.003}$	$0.84^{+0.01}_{-0.02}$	$0.085^{+0.013}_{-0.008}$
K2-53 b	$26.3^{+0.4}_{-0.4}$	$0.31^{+0.07}_{-0.10}$	$89.32^{+0.22}_{-0.16}$	$0.028^{+0.001}_{-0.001}$	$0.031^{+0.002}_{-0.002}$	$0.030^{+0.001}_{-0.001}$	−8.83	−6.61	$0.145^{+0.003}_{-0.003}$	$0.136^{+0.004}_{-0.003}$	$0.94^{+0.00}_{-0.00}$	$0.033^{+0.002}_{-0.002}$
205084841.01	$17.8^{+0.5}_{-0.6}$	$0.62^{+0.03}_{-0.03}$	$87.99^{+0.16}_{-0.17}$	$0.127^{+0.002}_{-0.002}$	$0.117^{+0.002}_{-0.002}$	$0.122^{+0.002}_{-0.002}$	−6.36	−5.25	$0.189^{+0.003}_{-0.002}$	$0.125^{+0.003}_{-0.003}$	$0.66^{+0.02}_{-0.02}$	$0.203^{+0.016}_{-0.014}$
K2-289 b	$22.5^{+0.3}_{-0.3}$	$0.60^{+0.02}_{-0.02}$	$88.48^{+0.07}_{-0.07}$	$0.081^{+0.001}_{-0.001}$	$0.082^{+0.001}_{-0.002}$	$0.081^{+0.001}_{-0.001}$	−7.42	−6.24	$0.168^{+0.002}_{-0.002}$	$0.130^{+0.002}_{-0.002}$	$0.77^{+0.01}_{-0.01}$	$0.128^{+0.005}_{-0.005}$
K2-174 b	$26.6^{+0.2}_{-0.2}$	$0.02^{+0.03}_{-0.02}$	$89.95^{+0.04}_{-0.05}$	$0.033^{+0.000}_{-0.000}$	$0.038^{+0.001}_{-0.001}$	$0.036^{+0.001}_{-0.001}$	−9.25	−6.80	$0.242^{+0.002}_{-0.002}$	$0.225^{+0.002}_{-0.002}$	$0.93^{+0.00}_{-0.00}$	$0.036^{+0.001}_{-0.001}$
K2-87 b	$14.4^{+0.3}_{-0.3}$	$0.57^{+0.03}_{-0.03}$	$87.74^{+0.17}_{-0.17}$	$0.045^{+0.001}_{-0.001}$	$0.055^{+0.002}_{-0.002}$	$0.050^{+0.001}_{-0.001}$	−7.84	−5.94	$0.190^{+0.002}_{-0.002}$	$0.164^{+0.003}_{-0.003}$	$0.86^{+0.01}_{-0.01}$	$0.074^{+0.005}_{-0.004}$
K2-90 b	$33.4^{+0.3}_{-0.3}$	$0.44^{+0.05}_{-0.05}$	$89.24^{+0.09}_{-0.09}$	$0.036^{+0.001}_{-0.001}$	$0.041^{+0.002}_{-0.002}$	$0.038^{+0.001}_{-0.001}$	−8.33	−6.37	$0.123^{+0.003}_{-0.003}$	$0.112^{+0.003}_{-0.003}$	$0.91^{+0.01}_{-0.01}$	$0.048^{+0.004}_{-0.003}$
K2-124 b	$28.0^{+1.5}_{-1.7}$	$0.47^{+0.10}_{-0.14}$	$89.03^{+0.32}_{-0.27}$	$0.069^{+0.002}_{-0.002}$	$0.068^{+0.003}_{-0.003}$	$0.069^{+0.002}_{-0.002}$	−6.89	−5.73	$0.070^{+0.002}_{-0.002}$	$0.058^{+0.003}_{-0.003}$	$0.84^{+0.02}_{-0.03}$	$0.089^{+0.016}_{-0.013}$

Note. Transit parameters derived from the simultaneous analysis of the *K2* and *Spitzer* data. The parameters $R_{p,K}$, $R_{p,S}$, and $R_{p,C}$ are the *K2*, *Spitzer*, and combined values of the planet radius in units of the stellar radius. The best-fit logarithms of the Gaussian errors for the *K2* and *Spitzer* time series are denoted by $\log(\sigma_K)$ and $\log(\sigma_S)$, respectively. The parameter η is the transit shape defined in Equation (5). The maximum planet radius allowed by the shape of the transit is denoted $R_{p,\max}$ and defined in Equation (6).

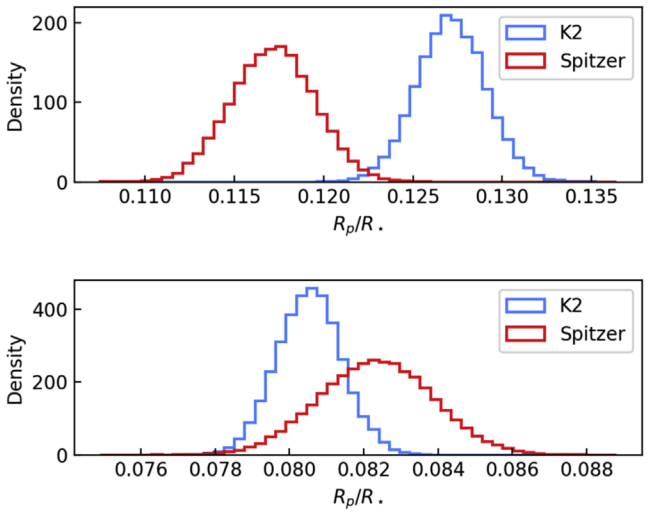

Figure 7. Marginalized posterior distributions of $R_p/R_\star$ in the *Kepler* and *Spitzer* bandpasses for EPIC 205084841.01 (top) and K2-289 b (bottom). In the case of EPIC 205084841.01, the disagreement casts doubt on the planetary hypothesis, while the agreement in the case of K2-289 b is consistent with a planet.

3.7. Stellar Parameters

We used the Python package `isochrones` to infer a uniform set of stellar parameters using priors from spectroscopy (when available), Two Micron All Sky Survey (2MASS) *JHK* photometry (Skrutskie et al. 2006), and *Gaia* DR2 parallaxes (Gaia Collaboration et al. 2016, 2018). We list the inputs to `isochrones` in Table 5. We sampled the posteriors using MultiNest (Feroz et al. 2013) in conjunction with the MIST stellar evolution models (Choi et al. 2016). The resulting posteriors are listed in Table 6.

3.8. Planet Validation

The open-source Python package `vespa` (Morton 2015b) has been used to validate planets via statistical FPPs in numerous recent works (e.g., Montet et al. 2015; Morton et al. 2016) and is similar to previous methods developed for *Kepler* and *CoRoT*, such as `BLENDER` (Torres et al. 2011) and `PASTIS` (Díaz et al. 2014). Cr16 used `vespa` to compute FPPs for planet candidates from *K2*'s first five observing campaigns, including those we analyze here (with the exception of K2-124 b). `vespa` uses the `TRILEGAL` Galaxy model (Girardi et al. 2005) to simulate populations of FP scenarios (i.e., eclipsing binaries [EBs], background EBs [BEBs], and hierarchical triple EB [HEB] systems) and then compares these to the observed phase-folded light curve to compute statistical likelihoods for each type of false FP, as well as the planetary scenario. For a more detailed description of how we use `vespa`, see Cr16.

In common practice among planet hunters, the "by-eye" transit shape is used as a first line of defense in the initial stages of vetting newly detected planet candidates in transit surveys: EBs are usually more obviously "V-shaped" than a planetary transit, as well as being deeper (in the absence of significant dilution). However, the 30-minute cadence of *K2* can make the transits of real planets appear more V-shaped, so a more quantitative assessment based on precise parameter estimates is more reliable. The ratio of the full transit duration (T_{23}) to the total transit duration (T_{14}) is directly determined by the transit geometry, regardless of dilution from any additional sources within the photometric aperture (Seager & Mallén-Ornelas 2003). We denote this ratio η, the transit "shape"—a number that scales between 0 and 1, where 0 corresponds to a "V-shaped" transit and 1 corresponds to a "box-shaped" transit:

$$\eta = \frac{T_{23}}{T_{14}}. \tag{5}$$

The transit shape thus sets an upper limit on $R_p/R_\star$:

$$R_{p,\max}/R_\star = \frac{1-\eta}{1+\eta}. \tag{6}$$

As $\eta \to 1$, $R_p/R_\star \to R_{p,\max}/R_\star$, meaning that the constraint is stronger for more "box-shaped" transits. This constraint can be particularly useful in the case of dilution from a known stellar companion (detected either photometrically or spectroscopically). `vespa` implicitly uses the shape information content of the phase-folded transit light curve to compute the likelihoods of FP and planet models. Thus, an independent consideration of FP scenarios is enabled by quantifying the shape η of each transit. Furthermore, a constraint on the maximum allowed dilution results directly from comparison of the observed values of $R_p/R_\star$ and $R_{p,\max}/R_\star$. The transit shape η and the maximum radius ratio $R_{p,\max}/R_\star$ are listed in Table 3, along with other parameters of interest.

Another useful constraint derived from the transit fit is the estimate of the mean stellar density. We compute this estimate of the stellar density directly from the observed transit light-curve fit parameters using Equation (4) of Kipping (2014):

$$\rho_{\star,\mathrm{LC}} = \frac{3\pi(a/R_\star)^3}{\mathrm{GP}^2}. \tag{7}$$

This estimate can then be compared directly to independent estimates of the mean stellar density, i.e., from spectroscopy. Significant disagreement could arise from the violation of any of the assumptions inherent to this estimate (i.e., non-negligible blending, a noncircular orbit, $M_p \sim M_\star$).

4. Discussion

4.1. Validation

The planets in our sample with established "validated" dispositions (K2-52 b, K2-53 b, K2-87 b, K2-90 b, Cr16; K2-124 b, Dressing et al. 2017; Livingston et al. 2018a; K2-174 b, Mayo et al. 2018) do not exhibit suspiciously chromatic transit depths that would indicate that they are actually FPs. With the exception of K2-174, our transit analyses (without density priors) yield mean stellar densities ($\rho_{\star,\mathrm{LC}}$) within 2σ of the values from our independent assessment (Section 3.7). This agreement provides an additional layer of confidence in the disposition of these planets, as well as the quality of our transit analysis and stellar characterization.

On the other hand, K2-174 b yields $\rho_{\star,\mathrm{LC}} = 0.53^{+0.23}_{-0.21}$ g cm^{-3}, which is $\sim 10\sigma$ discrepant with the value we derive for the host star, $\rho_\star = 3.21^{+0.15}_{-0.14}$ g cm^{-3}. Furthermore, the addition of a density prior does not significantly change this result, which indicates that the data strongly constrain the density to this value. We interpret this result as an indication of eccentricity in the system, which could potentially be measured via RVs (see Section 4.2).

Table 4
Ephemerides

Name	*K2*-only		*K2* + *Spitzer*		Mid-2021 Timing Uncertainty		Improvement[a]
	P (days)	T_0 (BKJD)	*P* (days)	T_0 (BKJD)	*K2*-only (hr)	*K2* + *Spitzer* (minutes)	
K2-52 b	$3.534890^{+0.000187}_{-0.000181}$	$2063.02742^{+0.00190}_{-0.00184}$	$3.535055^{+0.000017}_{-0.000016}$	$2063.02618^{+0.00108}_{-0.00111}$	3.1	17	11×
K2-53 b	$12.207253^{+0.000940}_{-0.000971}$	$2063.38751^{+0.00400}_{-0.00373}$	$12.207720^{+0.000123}_{-0.000113}$	$2063.38582^{+0.00189}_{-0.00186}$	4.7	35	8×
205084841.01	$11.310159^{+0.000564}_{-0.000557}$	$2060.85877^{+0.00224}_{-0.00221}$	$11.310099^{+0.000045}_{-0.000045}$	$2060.85913^{+0.00110}_{-0.00109}$	3.0	14	12×
K2-289 b	$13.157344^{+0.000622}_{-0.000634}$	$2064.14222^{+0.00205}_{-0.00198}$	$13.156969^{+0.000047}_{-0.000051}$	$2064.14325^{+0.00097}_{-0.00094}$	2.9	13	13×
K2-174 b	$19.564172^{+0.000996}_{-0.000966}$	$2250.77803^{+0.00100}_{-0.00099}$	$19.562307^{+0.000078}_{-0.000076}$	$2250.77917^{+0.00095}_{-0.00094}$	2.8	13	13×
K2-87 b	$9.726793^{+0.000663}_{-0.000646}$	$2239.30189^{+0.00229}_{-0.00242}$	$9.726618^{+0.000055}_{-0.000055}$	$2239.30232^{+0.00171}_{-0.00171}$	3.8	19	12×
K2-90 b	$13.733225^{+0.001206}_{-0.001187}$	$2245.66111^{+0.00185}_{-0.00190}$	$13.733314^{+0.000083}_{-0.000099}$	$2245.66112^{+0.00170}_{-0.00172}$	4.9	22	13×
K2-124 b	$6.413721^{+0.000271}_{-0.000272}$	$2309.18063^{+0.00187}_{-0.00182}$	$6.413651^{+0.000036}_{-0.000031}$	$2309.18106^{+0.00105}_{-0.00107}$	2.3	17	8×

Notes. BKJD is the Barycentric Julian Date offset by the beginning of the *Kepler* mission, i.e., BJD –2,454,833.
[a] Relative improvement in period measurement precision from our joint analysis of the *K2* and *Spitzer* data, as compared to *K2*-only.

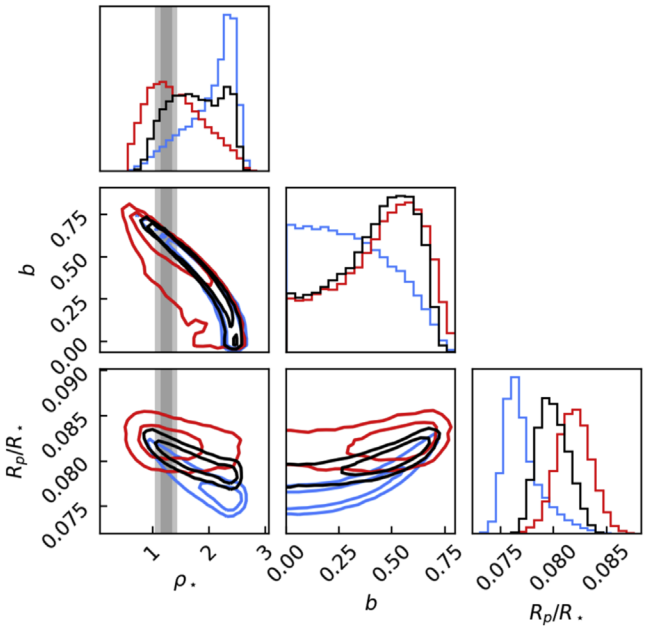

Figure 8. Marginalized posterior distributions for key system parameters of K2-289 b (without a prior on the mean stellar density), where the contours correspond to the 68% and 95% credible regions. The colors of the contours and histograms correspond to the data set analyzed: blue is *K2*-only, red is *Spitzer*-only, and black is simultaneous *K2*-*Spitzer*. The vertical gray bands show the 68% and 95% credible regions for the stellar density from our `isochrones` analysis.

In the next two subsections we examine the dispositions of the two previously unvalidated planet candidates in our sample, EPIC 205084841.01 and K2-289 b.

4.1.1. EPIC 205084841.01

EPIC 205084841.01 does not warrant validation at present, but neither should it be considered a "confirmed" FP; the current disposition of planet candidate is appropriate. Using the contrast curve derived from our Keck/NIRC2 AO image (see Figure 1), along with the `isochrones` inputs listed in Table 5, we compute an FPP of 15.4% for this target with `vespa`, somewhat higher than the FPP of 2.7% reported by Cr16, and significantly above the commonly used validation threshold of 1%. We discuss below several considerations pertinent to the disposition of this system.

Caution is warranted by the candidate's large radius of $\sim 17\,R_\oplus$, which is comparable to the radii of low-mass stars (Shporer et al. 2017). Additionally, there is moderate tension between $R_p/R_\star$ in the *Kepler* and *Spitzer* bandpasses (see Figure 7). The posterior of $R_p/R_\star$ is $\sim 3.3\sigma$ larger in the *Kepler* bandpass, which is consistent with an occultation by a lower-mass star. Although the FPP implies that the candidate is more likely a planet than an FP, `vespa` does not take into account chromaticity of transit depth. The second-most likely scenario reported by `vespa` is an EB, and `vespa` essentially rules out a hierarchical or background EB scenario.

Assuming that the candidate is actually an EB with the same orbital period, a secondary eclipse could be measurable in the *K2* data; the absence of any apparent secondary eclipses (deeper than ∼0.1% at any phase; see Figure 2) is therefore suggestive of an eccentric orbit. Our transit analysis (without a density prior) yields $\rho_{\star,\mathrm{LC}} = 1.43^{+0.29}_{-0.34}$ g cm^{-3}, which is 1.8σ higher than the value we measure for the host star (see Table 6) and thus modestly suggestive of eccentricity. There is no apparent variation in the transit depth, and the transit geometry implies a radius ratio much smaller than unity ($\lesssim$20%; see Table 3), so an EB at twice the estimated orbital period is unlikely. We conclude that EPIC 205084841.01 is potentially an FP caused by the eclipses of a low-mass star in an eccentric orbit, but further observations are required to confirm this scenario (e.g., RV monitoring); based on its FPP alone, the candidate is more likely to be an inflated gas giant planet.

4.1.2. K2-289 b

Cr16 reported an FPP of 1.3×10^{-11} for this candidate but did not validate the candidate owing to the presence of a nearby stellar companion revealed by AO imaging. Using the contrast curve for this star in Figure 1 and the `isochrones` inputs listed in Table 5, we find a higher (but still rather low) FPP of 3.7×10^{-4}. The companion is at a separation of 0.″8 and is 3.8 mag fainter (in *K* band) than the primary star. The 1.″2 pixel scale of IRAC is thus insufficient to resolve the companion in our follow-up *Spitzer* transit photometry. Intriguingly, the companion was not detected by *Gaia* DR2, but K2-289 is listed with zero excess astrometric noise, which is often associated

Table 5
Gaia DR2 Parallax, 2MASS Photometry, and Spectroscopic Priors Used to Estimate Stellar Parameters

EPIC	π (mas)	J (mag)	H (mag)	K (mag)	$T_{\rm eff}$ (K)	$\log g$ (cgs)	[Fe/H] (dex)	Note
203776696	0.9394 ± 0.1169	12.729 ± 0.026	12.126 ± 0.021	11.853 ± 0.019	...	...	...	...
204890128	7.2173 ± 0.1161	10.306 ± 0.024	9.826 ± 0.024	9.664 ± 0.021	5278 ± 100	4.546 ± 0.100	−0.03 ± 0.06	1
205084841	1.1594 ± 0.1117	13.443 ± 0.026	12.797 ± 0.026	12.612 ± 0.027	...	...	...	...
205686202	3.6170 ± 0.1037	11.435 ± 0.021	10.847 ± 0.022	10.641 ± 0.021	5365 ± 110	...	0.16 ± 0.08	3
210558622	9.9783 ± 0.1062	10.231 ± 0.021	9.649 ± 0.022	9.496 ± 0.017	4310 ± 70	...	0.11 ± 0.09	2
210731500	2.0071 ± 0.1040	11.811 ± 0.020	11.359 ± 0.022	11.197 ± 0.019	5694 ± 100	4.067 ± 0.100	0.36 ± 0.06	1
210968143	7.4234 ± 0.1026	11.168 ± 0.023	10.495 ± 0.027	10.360 ± 0.020	4465 ± 100	4.553 ± 0.100	−0.25 ± 0.06	1
212154564	7.0953 ± 0.1198	12.838 ± 0.023	12.227 ± 0.022	11.975 ± 0.018	3443 ± 70	...	−0.13 ± 0.09	2

Note. (1) Keck/HIRES `SpecMatch-syn`; (2) Keck/HIRES `SpecMatch-emp`; (3) Subaru/HDS `SpecMatch-emp`. Following Luri et al. (2018), we added 0.1 mas in quadrature to the Gaia DR2 parallax uncertainties to account for systematic errors.

Table 6
Stellar Parameters

EPIC	$T_{\rm eff}$ (K)	$\log g$ (cgs)	[Fe/H] (dex)	$M_\star$ ($M_\odot$)	$R_\star$ ($R_\odot$)	Distance (pc)	$\rho_\star$ (cgs)
203776696	7147^{+483}_{-506}	$3.979^{+0.087}_{-0.085}$	$0.055^{+0.154}_{-0.139}$	$1.691^{+0.157}_{-0.143}$	$2.192^{+0.280}_{-0.232}$	$1041.7^{+132.7}_{-104.1}$	$0.22^{+0.08}_{-0.06}$
204890128	5263^{+88}_{-86}	$4.555^{+0.022}_{-0.028}$	$-0.037^{+0.052}_{-0.053}$	$0.851^{+0.032}_{-0.038}$	$0.807^{+0.016}_{-0.015}$	$139.1^{+2.2}_{-2.0}$	$2.29^{+0.15}_{-0.18}$
205084841	6245^{+369}_{-284}	$4.271^{+0.062}_{-0.066}$	$0.019^{+0.150}_{-0.175}$	$1.168^{+0.120}_{-0.094}$	$1.313^{+0.126}_{-0.113}$	$860.4^{+84.1}_{-76.4}$	$0.73^{+0.18}_{-0.16}$
205686202	5529^{+77}_{-74}	$4.393^{+0.024}_{-0.022}$	$0.162^{+0.087}_{-0.074}$	$0.953^{+0.037}_{-0.051}$	$1.025^{+0.030}_{-0.028}$	$270.7^{+7.6}_{-7.1}$	$1.24^{+0.10}_{-0.09}$
210558622	4455^{+31}_{-29}	$4.625^{+0.017}_{-0.017}$	$0.113^{+0.065}_{-0.071}$	$0.700^{+0.025}_{-0.023}$	$0.676^{+0.008}_{-0.008}$	$100.1^{+1.0}_{-1.0}$	$3.21^{+0.15}_{-0.14}$
210731500	5747^{+58}_{-49}	$4.208^{+0.032}_{-0.035}$	$0.328^{+0.051}_{-0.045}$	$1.164^{+0.042}_{-0.044}$	$1.401^{+0.083}_{-0.062}$	$503.6^{+29.9}_{-21.9}$	$0.59^{+0.07}_{-0.08}$
210968143	4484^{+58}_{-50}	$4.653^{+0.017}_{-0.014}$	$-0.225^{+0.053}_{-0.053}$	$0.629^{+0.022}_{-0.018}$	$0.619^{+0.009}_{-0.010}$	$134.9^{+1.7}_{-1.7}$	$3.74^{+0.19}_{-0.14}$
212154564	3570^{+63}_{-70}	$4.858^{+0.012}_{-0.088}$	$0.023^{+0.061}_{-0.106}$	$0.390^{+0.013}_{-0.042}$	$0.388^{+0.016}_{-0.009}$	$140.4^{+2.3}_{-2.3}$	$9.58^{+0.47}_{-2.12}$

with binarity (see, e.g., Evans 2018). This underscores the need for high-resolution imaging, even in the *Gaia* era.

From our AO imaging (Section 2.3), we compute deblended J-band magnitudes of 11.461 ± 0.024 and 15.554 ± 0.055 for the primary and secondary stars, respectively; in K band the deblended magnitudes are 10.674 ± 0.021 and 14.446 ± 0.024. The $J-K$ color of the secondary star is thus 1.108 ± 0.060, which is consistent with a late M dwarf.

From the observed transit depth, an EB with 100% eclipse depth that is less than 5.4 mag fainter than the primary could reproduce the observed transit depth. However, the $J-K$ color of the companion suggests that it is a late M dwarf, so the contrast in the *Kepler* bandpass should be $\gtrsim$4 mag greater than in K band. In this likely scenario, we can rule out the secondary as the source of the signal, as the dilution from the primary star in the *Kepler* bandpass would require a depth larger than 100%. Furthermore, we can leverage our measurement of the transit geometry to eliminate considerations of the secondary star's spectral type. From our joint analysis of the *K2* and *Spitzer* data, we have the constraint $R_{p,\rm max}/R_\star < 0.153$ (5σ), which corresponds to a maximum undiluted transit depth of ∼2.3%. Given the observed transit depth, this translates to an upper limit on the amount of dilution of about 1 mag. The secondary star would thus need to have a nonphysical color of $V-K \lesssim -2.8$ to be the source of the signal. We therefore conclude that the observed signal comes from the primary star.

From the above considerations we can confidently rule out scenarios in which the signal comes from the secondary source, i.e., the signal is due to a BEB or eclipsing HEB. We now consider the possibility that the primary is itself an EB. While low-mass stars can potentially be roughly Jovian in size, such massive bodies would induce a large-amplitude Doppler signal in time-series RV measurements of the primary star, as well as potentially significant secondary eclipses.

The RVs obtained with Subaru/HDS (see Section 2.4) show no significant variation on a timescale of ∼3 days, ruling out the possibility that K2-289 is an EB. Assuming a circular orbit, we used `RadVel` to estimate the RV semi-amplitude exerted by the transiting companion as $K = 0.03^{+5.47}_{-0.03}\,{\rm m\,s^{-1}}$, which is consistent with a null detection. The semi-amplitude best-fit value and 3σ upper limit are 11.8 and 46.1 $\rm m\,s^{-1}$, respectively. This result is consistent with the `vespa` result, as well as our assessment of the *K2* and *Spitzer* transit data, which both suggest a planetary origin for the observed transit signal, so we conclude that this is a valid planet.

Since we do not account for the dilution from the companion in our transit fits, the planet radius we measure may be underestimated. However, the delta-magnitude of 3.82 (in K band) implies a planet radius only ∼1.5% larger than we list in Table 7, which is a factor of ∼6 smaller than the precision of our planet radius measurement. Furthermore, the dilution is likely to be lower in *Kepler* band than K band, given that the secondary is probably a bound late-type companion. Future studies may yield precise enough measurements of $R_p/R_\star$ that dilution from the companion will need to be accounted for.

4.2. Potential for Characterization

In order to assess the potential for future characterization studies of these planets, we computed their physical properties using the parameter estimates from our transit analyses in Tables 3 and 4, as well as the stellar parameters in Table 6. We first computed updated planet radii and used the probabilistic mass–radius relation of Wolfgang et al. (2016) to predict the masses of these planets. We then computed the orbital

Table 7
Derived Planet Properties

Name	R_p ($R_\oplus$)	M_p ($M_\oplus$)	$K_{\rm pred}$ (m s^{-1})	a (au)	$T_{\rm eq}$ (K)	g ($g_\oplus$)	H (km)	$\delta_{\rm TS}$ (ppm)
K2-52 b	18.0 ± 2.2	128.6 ± 109.9	38.1 ± 32.6	0.054 ± 0.002	2004 ± 184	0.4	2129	1049
K2-53 b	2.6 ± 0.1	9.2 ± 2.5	2.8 ± 0.8	0.098 ± 0.001	665 ± 13	1.3	211	112
205084841.01	17.5 ± 1.7	123.4 ± 96.3	31.8 ± 25.0	0.104 ± 0.003	979 ± 73	0.4	1029	1374
K2-289 b	9.1 ± 0.3	48.6 ± 18.6	13.6 ± 5.2	0.107 ± 0.001	753 ± 16	0.6	545	623
K2-174 b	2.6 ± 0.1	9.2 ± 2.5	2.8 ± 0.8	0.126 ± 0.001	455 ± 5	1.3	145	110
K2-87 b	7.6 ± 0.4	37.9 ± 12.7	10.3 ± 3.4	0.094 ± 0.001	979 ± 28	0.7	633	323
K2-90 b	2.6 ± 0.1	9.0 ± 2.5	3.3 ± 0.9	0.096 ± 0.001	502 ± 8	1.4	157	139
K2-124 b	2.9 ± 0.1	10.5 ± 2.6	6.8 ± 1.8	0.049 ± 0.002	442 ± 17	1.2	151	383

Note. M_p comes from the probabilistic mass–radius relation of Wolfgang et al. (2016); we apply this relation uniformly for the sake of homogeneity, but note that M_p (and its uncertainty) may be underestimated for the larger planets in our sample. $K_{\rm pred}$ is the predicted RV semi-amplitude, a is semimajor axis, and $T_{\rm eq}$ is equilibrium temperature assuming a Bond albedo of 0.3; the uncertainties in these parameters propagate from the formal transit and stellar parameter estimates but are likely underestimated owing to uncertainties in the underlying models and assumptions. g is surface gravity, H is atmospheric scale height, and $\delta_{\rm TS}$ is the predicted amplitude of atmospheric features accessible via transmission spectroscopy; these estimates have large uncertainties owing to a number of factors, such as uncertainties in the stellar parameters, unknown planet masses, and assumed atmospheric compositions.

semimajor axis (in physical units), predicted RV semi-amplitude (assuming circular orbits), equilibrium temperature (assuming a Bond albedo of 0.3), surface gravity, and atmospheric scale height (assuming a hydrogen-dominated atmosphere, i.e., a mean molecular weight of 2). Finally, we used the formalism of Miller-Ricci et al. (2009) to estimate the amplitude of features in the planets' transmission spectra. We list these derived planet properties in Table 7.

K2-53 and K2-174 are moderately bright in the optical ($Kp \sim 12$), and each hosts an $R_p \sim 2.7\,R_\oplus$ planet with a predicted RV semi-amplitude of $K_{\rm pred} \sim 3\,{\rm m\,s^{-1}}$. These are thus potentially good targets for precision RV mass measurements with current optical spectrographs such as HIRES and HARPs, which would enable studies of the densities and bulk composition of temperate sub-Neptunes. K2-289 b and K2-87 b are both sub-Saturns orbiting moderately IR-bright stars ($J < 12$) with $K_{\rm pred} = 13.6 \pm 5.2$ and $K_{\rm pred} = 10.3 \pm 3.4\,{\rm m\,s^{-1}}$, respectively, making them good targets for one of the high-precision "red" (IR) spectrographs currently under development (e.g., Subaru/IRD, Tamura et al. 2012; Spirou, Artigau et al. 2014; HPF, Mahadevan et al. 2015). Mass measurements for these planets would add crucial data points to the relatively small population of similarly sized planets with well-measured densities, which exhibit a diverse range of core mass fractions (Petigura et al. 2017). K2-90 and K2-124 are similarly IR-bright but host temperate sub-Neptunes with $K_{\rm pred} = 3$–$6\,{\rm m\,s^{-1}}$, making them also potentially interesting targets for red spectrographs.

Due to the small size and moderate infrared brightness of the host star, K2-124 b could be an interesting target for atmospheric studies via transmission spectroscopy with *JWST*. The predicted amplitude of features in the planet's transmission spectrum would be roughly 350 ppm (with large uncertainties owing to the unknown planet mass and atmospheric mean molecular weight). By combining multiple transit observations, these features should be detectable with *JWST*. This $2.5\,R_\oplus$ planet receives only ∼8 times the incident radiation as Earth, so such studies would probe the atmospheric properties of temperate sub-Neptunes.

The combination of *K2* and *Spitzer* data in this work demonstrates the synergy between transit detection and follow-up with space-based instruments. Because *TESS* has a pixel scale five times larger than *Kepler* (21″ vs. 4″), the frequency of stellar blends will likely be significantly larger, which will increase the utility of transit follow-up. The upcoming *CHEOPS* mission has a similar pixel scale to *Spitzer* and will thus prove useful for *TESS* follow-up in much the same way that *Spitzer* has for *K2*.

5. Summary

We have used *Spitzer* to observe the transits of eight planet candidates discovered by *K2*, and we perform a global analysis of the light curves from both telescopes. The value of *Spitzer* follow-up transit observations of *K2* candidates is twofold—the high-cadence infrared light curves allow a finer sampling of the transit shape, which is less confounded by uncertain limb darkening, and the measurement of an additional transit time at a later epoch yields a more precise estimate of the ephemeris. Our follow-up transit observations with *Spitzer* demonstrate the utility of transit follow-up observations for planet validation and ephemeris refinement, paving the way for future RV and atmospheric studies. These observations reduce mid-2021 transit timing uncertainties by ∼90%, thus enabling efficient scheduling with *JWST*.

This work is based in part on observations made with the *Spitzer Space Telescope*, which is operated by the Jet Propulsion Laboratory, California Institute of Technology (Caltech), under contract with the National Aeronautics and Space Administration (NASA). This paper includes data collected by the *K2* mission. Funding for the *K2* mission is provided by the NASA Science Mission directorate. This work benefited from the Exoplanet Summer Program in the Other Worlds Laboratory (OWL) at the University of California, Santa Cruz, a program funded by the Heising-Simons Foundation. E.S. is supported by a postgraduate scholarship from the Natural Sciences and Engineering Research Council of Canada. E.A.P. acknowledges support by NASA through a Hubble Fellowship grant awarded by the Space Telescope Science Institute, which is operated by the Association of Universities for Research in Astronomy, Inc., for NASA, under contract NAS 5-26555. A.W.H. acknowledges support for our *K2* team through a NASA Astrophysics Data Analysis Program grant. A.W.H. and I.J.M.C. acknowledge support from the K2 Guest Observer Program. This work was performed (in part) under contract with the Jet Propulsion Laboratory (JPL) funded

Table 8
Limb-darkening Priors

Name	*K2*		*Spitzer*	
	q_1	q_2	q_1	q_2
K2-52	$\mathcal{N}(0.339, 0.024)$	$\mathcal{N}(0.237, 0.030)$	$\mathcal{N}(0.026, 0.005)$	$\mathcal{N}(0.174, 0.022)$
K2-53	$\mathcal{N}(0.490, 0.012)$	$\mathcal{N}(0.372, 0.016)$	$\mathcal{N}(0.047, 0.002)$	$\mathcal{N}(0.198, 0.019)$
205084841	$\mathcal{N}(0.392, 0.034)$	$\mathcal{N}(0.271, 0.028)$	$\mathcal{N}(0.035, 0.005)$	$\mathcal{N}(0.165, 0.023)$
K2-289	$\mathcal{N}(0.481, 0.011)$	$\mathcal{N}(0.339, 0.012)$	$\mathcal{N}(0.043, 0.002)$	$\mathcal{N}(0.203, 0.023)$
K2-174	$\mathcal{N}(0.561, 0.007)$	$\mathcal{N}(0.463, 0.005)$	$\mathcal{N}(0.055, 0.001)$	$\mathcal{N}(0.213, 0.019)$
K2-87	$\mathcal{N}(0.453, 0.008)$	$\mathcal{N}(0.327, 0.007)$	$\mathcal{N}(0.043, 0.001)$	$\mathcal{N}(0.153, 0.015)$
K2-90	$\mathcal{N}(0.553, 0.003)$	$\mathcal{N}(0.448, 0.003)$	$\mathcal{N}(0.058, 0.001)$	$\mathcal{N}(0.205, 0.021)$
K2-124	$\mathcal{N}(0.530, 0.023)$	$\mathcal{N}(0.266, 0.029)$	$\mathcal{N}(0.038, 0.001)$	$\mathcal{N}(0.082, 0.036)$

by NASA through the Sagan Fellowship Program executed by the NASA Exoplanet Science Institute. This research has made use of the NASA Exoplanet Archive, which is operated by Caltech, under contract with NASA's Exoplanet Exploration Program. This work made use of the SIMBAD database (operated at CDS, Strasbourg, France) and NASA's Astrophysics Data System Bibliographic Services. This research made use of the Infrared Science Archive, which is operated by Caltech, under contract with NASA. Portions of this work were performed at the California Institute of Technology under contract with NASA. Some of the data presented herein were obtained at the W. M. Keck Observatory, which is operated as a scientific partnership between Caltech, the University of California, and NASA. The authors wish to extend special thanks to those of Hawai'ian ancestry, on whose sacred mountain of Maunakea we are privileged to be quests. We are most fortunate to have the opportunity to conduct observations from this mountain.

Facilities: Kepler, *Spitzer*, *Gaia*, Keck (NIRC2, HIRES), Subaru (HDS).

Software: `numpy` (Oliphant 2006), `scipy` (Jones et al. 2001), `matplotlib` (Hunter 2007), `lmfit` (Newville et al. 2014), `emcee` (Foreman-Mackey et al. 2013), `celerite` (Foreman-Mackey et al. 2017), `batman` (Kreidberg 2015), `isochrones` (Morton 2015a), `vespa`, (Morton 2015b), `k2phot` (Petigura et al. 2015), `SpecMatch-syn` (Petigura 2015), `SpecMatch-emp` (Yee et al. 2017b), `RadVel` (Fulton et al. 2018), `IRAF` (Tody 1986, 1993).

Appendix
Limb Darkening

We used Gaussian limb-darkening priors in our transit analysis of the *K2* and *Spitzer* data (see Section 3.4). We use our stellar parameter estimates to determine these priors, so the more uncertain our knowledge of the host star, the less informative these priors are. Our Gaussian priors have typical widths of ∼10%, which is comparable to the uncertainty from the stellar limb-darkening models (e.g., Csizmadia et al. 2013; Müller et al. 2013). In practice, these priors do not have a large effect on the final results, especially in the case of the *Spitzer* data, where limb darkening is almost negligible at 4.5 μm. Conversely, the light curves are not sufficient to constrain limb darkening empirically—the photometric precision of the *Spitzer* data is too low, and the cadence of the *K2* data is too long. As a result, the posteriors of the limb-darkening parameters are nearly identical to the priors. We list the limb-darkening priors used in our analyses in Table 8.

Table 9
The Effect of the Choice of Limb-darkening Law on Estimates of $R_p/R_\star$, for a Range of Host Star Effective Temperatures

Name	$R_{p,K}$ ($R_\star$)	$R_{p,S}$ ($R_\star$)
Linear		
205084841.01	$0.12171^{+0.00231}_{-0.00187}$	$0.11602^{+0.00237}_{-0.00225}$
K2-174 b	$0.03605^{+0.00244}_{-0.00179}$	$0.03892^{+0.00129}_{-0.00143}$
K2-124 b	$0.06791^{+0.00398}_{-0.00255}$	$0.07005^{+0.00373}_{-0.00318}$
Quadratic		
205084841.01	$0.12134^{+0.00208}_{-0.00179}$	$0.11616^{+0.00223}_{-0.00248}$
K2-174 b	$0.03593^{+0.00301}_{-0.00160}$	$0.03864^{+0.00129}_{-0.00133}$
K2-124 b	$0.06761^{+0.00333}_{-0.00226}$	$0.07011^{+0.00317}_{-0.00342}$
Square root		
205084841.01	$0.12187^{+0.00215}_{-0.00202}$	$0.11586^{+0.00246}_{-0.00232}$
K2-174 b	$0.03615^{+0.00284}_{-0.00183}$	$0.03868^{+0.00131}_{-0.00130}$
K2-124 b	$0.06770^{+0.00367}_{-0.00243}$	$0.06994^{+0.00326}_{-0.00329}$
Logarithmic		
205084841.01	$0.12134^{+0.00197}_{-0.00172}$	$0.11584^{+0.00246}_{-0.00229}$
K2-174 b	$0.03597^{+0.00260}_{-0.00180}$	$0.03881^{+0.00124}_{-0.00137}$
K2-124 b	$0.06774^{+0.00374}_{-0.00219}$	$0.07043^{+0.00324}_{-0.00340}$

Note. The subscripts K and S denote the *Kepler* and *Spitzer* (4.5 μm) bandpasses, respectively.

The choice of limb-darkening law can potentially affect the posteriors of system parameters, due to deficiencies in the parameterization of the underlying flux variations across the stellar disk (e.g., Espinoza & Jordán 2016; Morello et al. 2017). We tested the effect of using a quadratic limb-darkening law by repeating our analysis of the *K2* and *Spitzer* data for three host stars spanning a range of effective temperatures, using a range of limb-darkening laws. Specifically, we tested a total of four different limb-darkening laws: linear, quadratic, square root, and logarithmic. For each limb-darkening law, we computed priors for the limb-darkening coefficients via Monte Carlo interpolation of the appropriate tables of Claret et al. (2012), enabling uncertainties in stellar parameters to propagate to uncertainties in the limb-darkening parameters for each law, as well as helping to ensure that only physical limb-darkening solutions are considered during MCMC. We list the posteriors of $R_p/R_\star$ in the *Kepler* and *Spitzer* 4.5 μm bands for EPIC 205084841 (∼6250 K), K2-174 (∼4450 K), and K2-124 (∼3570 K) in Table 9. As no significant differences in the estimates of $R_p/R_\star$ can be seen in either bandpass, we conclude that the choice of limb-darkening law is not important in the

case of these data sets. A combination of high photometric precision and high cadence, e.g., *Kepler* short-cadence data, is likely necessary in order to observe significant dependence of transit parameter estimates on the choice of limb-darkening law.

ORCID iDs

John H. Livingston https://orcid.org/0000-0002-4881-3620
Erik A. Petigura https://orcid.org/0000-0003-0967-2893
Courtney D. Dressing https://orcid.org/0000-0001-8189-0233
Benjamin J. Fulton https://orcid.org/0000-0003-3504-5316
Teruyuki Hirano https://orcid.org/0000-0003-3618-7535
Joshua E. Schlieder https://orcid.org/0000-0001-5347-7062
Evan Sinukoff https://orcid.org/0000-0002-5658-0601
Molly Kosiarek https://orcid.org/0000-0002-6115-4359
Rachel Akeson https://orcid.org/0000-0001-9674-1564
Jessie L. Christiansen https://orcid.org/0000-0002-8035-4778
Andrew W. Howard https://orcid.org/0000-0001-8638-0320
Howard Isaacson https://orcid.org/0000-0002-0531-1073
Arturo O. Martinez https://orcid.org/0000-0002-3311-4085
Bun'ei Sato https://orcid.org/0000-0001-8033-5633
Motohide Tamura https://orcid.org/0000-0002-6510-0681

References

Artigau, É., Kouach, D., Donati, J.-F., et al. 2014, Proc. SPIE, 9147, 914715
Beichman, C., Livingston, J., Werner, M., et al. 2016, ApJ, 822, 39
Benneke, B., Werner, M., Petigura, E., et al. 2017, ApJ, 834, 187
Byrd, R., Lu, P., Nocedal, J., & Zhu, C. 1995, SIAM Journal of Scientific Computing, 16, 1190
Chen, G., Knutson, H. A., Dressing, C. D., et al. 2018, arXiv:1801.10177
Choi, J., Dotter, A., Conroy, C., et al. 2016, ApJ, 823, 102
Ciardi, D. R., Crossfield, I. J. M., Feinstein, A. D., et al. 2018, AJ, 155, 10
Claret, A., Hauschildt, P. H., & Witte, S. 2012, yCat, 354, 0
Coelho, P., Barbuy, B., Meléndez, J., Schiavon, R. P., & Castilho, B. V. 2005, A&A, 443, 735
Crossfield, I. J. M., Ciardi, D. R., Petigura, E. A., et al. 2016, ApJS, 226, 7
Csizmadia, S., Pasternacki, T., Dreyer, C., et al. 2013, A&A, 549, A9
David, T. J., Conroy, K. E., Hillenbrand, L. A., et al. 2016a, AJ, 151, 112
David, T. J., Hillenbrand, L. A., Petigura, E. A., et al. 2016b, Natur, 534, 658
Deming, D., Knutson, H., Kammer, J., et al. 2015, ApJ, 805, 132
Díaz, R. F., Almenara, J. M., Santerne, A., et al. 2014, MNRAS, 441, 983
Dressing, C. D., Sinukoff, E., Fulton, B. J., et al. 2018, AJ, 156, 70
Dressing, C. D., Vanderburg, A., Schlieder, J. E., et al. 2017, AJ, 154, 207
Espinoza, N., & Jordán, A. 2016, MNRAS, 457, 3573
Evans, D. F. 2018, RNAAS, 2, 20
Fazio, G. G., Hora, J. L., Willner, S. P., et al. 1998, Proc. SPIE, 3354, 1024
Feroz, F., Hobson, M. P., Cameron, E., & Pettitt, A. N. 2013, arXiv:1306.2144
Foreman-Mackey, D., Agol, E., Ambikasaran, S., & Angus, R. 2017, AJ, 154, 220
Foreman-Mackey, D., Hogg, D. W., Lang, D., & Goodman, J. 2013, PASP, 125, 306
Foreman-Mackey, D., Montet, B. T., Hogg, D. W., et al. 2015, ApJ, 806, 215
Fortier, A., Beck, T., Benz, W., et al. 2014, Proc. SPIE, 9143, 91432J
Fulton, B. J., Petigura, E. A., Blunt, S., & Sinukoff, E. 2018, PASP, 130, 044504
Gaia Collaboration, Brown, A. G. A., Vallenari, A., et al. 2018, A&A, 616, A1
Gaia Collaboration, Prusti, T., de Bruijne, J. H. J., et al. 2016, A&A, 595, A1
Gaidos, E., Mann, A. W., Rizzuto, A., et al. 2017, MNRAS, 464, 850
Gardner, J. P., Mather, J. C., Clampin, M., et al. 2006, SSRv, 123, 485
Gibson, N. P., Aigrain, S., Roberts, S., et al. 2012, MNRAS, 419, 2683
Girardi, L., Groenewegen, M. A. T., Hatziminaoglou, E., & da Costa, L. 2005, A&A, 436, 895
Goodman, J., & Weare, J. 2010, Communications in Applied Mathematics and Computational Science, 5, 65
Grillmair, C. J., Carey, S. J., Stauffer, J. R., et al. 2012, Proc. SPIE, 8448, 84481I
Howell, S. B., Sobeck, C., Haas, M., et al. 2014, PASP, 126, 398
Hunter, J. D. 2007, CSE, 9, 90
Ingalls, J. G., Krick, J. E., Carey, S. J., et al. 2012, Proc. SPIE, 8442, 84421Y
Ingalls, J. G., Krick, J. E., Carey, S. J., et al. 2016, AJ, 152, 44
Jones, E., Oliphant, T., Peterson, P., et al. 2001–present, SciPy: Open Source Scientific Tools for Python, http://www.scipy.org/
Kipping, D. M. 2013, MNRAS, 435, 2152
Kipping, D. M. 2014, MNRAS, 440, 2164
Knutson, H. A., Lewis, N., Fortney, J. J., et al. 2012, ApJ, 754, 22
Kreidberg, L. 2015, PASP, 127, 1161
Lanotte, A. A., Gillon, M., Demory, B. O., et al. 2014, A&A, 572, A73
Lewis, N. K., Knutson, H. A., Showman, A. P., et al. 2013, ApJ, 766, 95
Livingston, J. H., Crossfield, I. J. M., Petigura, E. A., et al. 2018a, AJ, 156, 277
Livingston, J. H., Dai, F., Hirano, T., et al. 2018b, AJ, 155, 115
Livingston, J. H., Dai, F., Hirano, T., et al. 2019, MNRAS, 484, 8
Livingston, J. H., Endl, M., Dai, F., et al. 2018c, AJ, 156, 78
Luri, X., Brown, A. G. A., Sarro, L. M., et al. 2018, A&A, 616, A9
Mahadevan, S., Ramsey, L. W., Terrien, R., et al. 2015, AAS Meeting, 225, 258.23
Mandel, K., & Agol, E. 2002, ApJL, 580, L171
Mann, A. W., Gaidos, E., Mace, G. N., et al. 2016a, ApJ, 818, 46
Mann, A. W., Gaidos, E., Vanderburg, A., et al. 2017, AJ, 153, 64
Mann, A. W., Newton, E. R., Rizzuto, A. C., et al. 2016b, AJ, 152, 61
Mann, A. W., Vanderburg, A., Rizzuto, A. C., et al. 2018, AJ, 155, 4
Mayo, A. W., Vanderburg, A., Latham, D. W., et al. 2018, AJ, 155, 136
Miller-Ricci, E., Seager, S., & Sasselov, D. 2009, ApJ, 690, 1056
Montet, B. T., Morton, T. D., Foreman-Mackey, D., et al. 2015, ApJ, 809, 25
Morello, G., Tsiaras, A., Howarth, I. D., & Homeier, D. 2017, AJ, 154, 111
Morton, T. D. 2015a, Isochrones: Stellar Model Grid Package, Astrophysics Source Code Library, ascl:1503.010
Morton, T. D. 2015b, VESPA: False Positive Probabilities Calculator, Astrophysics Source Code Library, ascl:1503.011
Morton, T. D., Bryson, S. T., Coughlin, J. L., et al. 2016, ApJ, 822, 86
Müller, H. M., Huber, K. F., Czesla, S., Wolter, U., & Schmitt, J. H. M. M. 2013, A&A, 560, A112
Nelder, J. A., & Mead, R. 1965, CompJ, 7, 308
Newville, M., Stensitzki, T., Allen, D. B., & Ingargiola, A. 2014, LMFIT: Non-Linear Least-Square Minimization and Curve-Fitting for Python, Zenodo, doi:https://doi.org/10.5281/zenodo.11813
Obermeier, C., Henning, T., Schlieder, J. E., et al. 2016, AJ, 152, 223
Oliphant, T. E. 2006, A Guide to NumPy (USA: Trelgol Publishing), http://www.numpy.org
Pepper, J., Gillen, E., Parviainen, H., et al. 2017, AJ, 153, 177
Petigura, E. A. 2015, PhD thesis, Univ. California, Berkeley
Petigura, E. A., Crossfield, I. J. M., Isaacson, H., et al. 2018, AJ, 155, 21
Petigura, E. A., Schlieder, J. E., Crossfield, I. J. M., et al. 2015, ApJ, 811, 102
Petigura, E. A., Sinukoff, E., Lopez, E. D., et al. 2017, AJ, 153, 142
Pont, F., Zucker, S., & Queloz, D. 2006, MNRAS, 373, 231
Rasmussen, C. E., & Williams, C. K. I. 2005, Gaussian Processes for Machine Learning (Cambridge, MA: MIT Press)
Ricker, G. R., Winn, J. N., Vanderspek, R., et al. 2015, JATIS, 1, 014003
Rizzuto, A. C., Vanderburg, A., Mann, A. W., et al. 2018, AJ, 156, 195
Sato, B., Hartman, J. D., Bakos, G. Á., et al. 2012, PASJ, 64, 97
Sato, B., Kambe, E., Takeda, Y., Izumiura, H., & Ando, H. 2002, PASJ, 54, 873
Seager, S., & Mallén-Ornelas, G. 2003, ApJ, 585, 1038
Shporer, A., Zhou, G., Vanderburg, A., et al. 2017, ApJL, 847, L18
Skrutskie, M. F., Cutri, R. M., Stiening, R., et al. 2006, AJ, 131, 1163
Tamura, M., Suto, H., Nishikawa, J., et al. 2012, Proc. SPIE, 8446, 84461T
Tody, D. 1986, Proc. SPIE, 627, 733
Tody, D. 1993, in ASP Conf. Ser. 52, Astronomical Data Analysis Software and Systems II, ed. R. J. Hanisch, R. J. V. Brissenden, & J. Barnes (San Francisco, CA: ASP), 173
Torres, G., Fressin, F., Batalha, N. M., et al. 2011, ApJ, 727, 24
Vanderburg, A., Latham, D. W., Buchhave, L. A., et al. 2016, ApJS, 222, 14
Vogt, S. S., Allen, S. L., Bigelow, B. C., et al. 1994, Proc. SPIE, 2198, 362
Werner, M. W., Roellig, T. L., Low, F. J., et al. 2004, ApJS, 154, 1
Winn, J. N., Holman, M. J., Torres, G., et al. 2008, ApJ, 683, 1076
Wizinowich, P., Smith, R., Biasi, R., et al. 2014, Proc. SPIE, 9148, 91482B
Wolfgang, A., Rogers, L. A., & Ford, E. B. 2016, ApJ, 825, 19
Yee, S. W., Petigura, E. A., & von Braun, K. 2017a, ApJ, 836, 77
Yee, S. W., Petigura, E. A., & von Braun, K. 2017b, yCat, 836, 0
Zhu, C., Byrd, R. H., Lu, P., & Nocedal, J. 1997, ACM Trans. Math. Softw., 23, 550